Materials Horizons

ROYAL SOCIETY OF CHEMISTRY

COMMUNICATION

View Article Online
View Journal

Cite this: DOI: 10.1039/d5mh00585j

Received 1st April 2025,
Accepted 13th June 2025

DOI: 10.1039/d5mh00585j

rsc.li/materials-horizons

Magnesium hydride-induced hydrogen therapy for enhanced sonodynamic therapy†

Jing Huang,[ad] Jianping Meng,[ad] Yijie Fan,[ad] Engui Wang,[d] Xiangxiang Wang,[ad] Huirun Fan,[e] Dan Luo,[ad] Lingling Xu*[d] and Zhou Li*[bc]

The tumor microenvironment (TME) is typically immunosuppressive, playing a crucial role in tumor progression, immune evasion, and therapeutic resistance, all of which significantly impede the efficacy of cancer therapies[1]. Herein, we propose that magnesium hydride (MgH_2)-induced hydrogen (H_2) therapy can synergistically enhance barium titanate (BTO)-mediated sonodynamic therapy (SDT) while modulating the TME to improve the efficacy of immune checkpoint inhibitors (aPD-1). Specifically, ultrasound (US) activated BTO to trigger SDT and induce immunogenic cell death (ICD), while the sustained release of H_2 from MgH_2 microspheres amplifies tumor cell destruction, thereby promoting immune cell recruitment to the tumor site. Meanwhile, the hydroxide ions (OH^-) and magnesium ions (Mg^{2+}) generated by MgH_2 alleviate the acidic TME, reversing immune suppression and enhancing T-cell-mediated antitumor responses. In the CT26 tumor model, the synergistic combination of SDT and MgH_2 therapy significantly enhances the anti-tumor efficacy of SDT compared to that of BTO alone, leading to prolonged survival of treated mice. Moreover, MgH_2 upregulates PD-1 expression in T cells, markedly improving the sensitivity of tumors to aPD-1 therapy. This strategy provides a generalizable approach for enhancing SDT, demonstrating its broad potential in anti-tumor treatment and presenting a promising avenue for overcoming resistance to immune checkpoint inhibitors.

New concepts

Malignant tumors impose a huge physical, psychological and economic burden on patients, while traditional methods are associated with severe side effects, harsh application conditions and drug resistance. Accordingly, new anti-tumor therapies with characteristics such as independence from tumor type, non-invasiveness and high safety have emerged. However, the efficiency of SDT is severely affected by the TME. The TME is usually immunosuppressive and plays a crucial role in tumor progression, immune evasion and treatment resistance. Therefore, we proposed a combined therapeutic strategy (BUM) based on hydrogen therapy and sonodynamic therapy. MgH_2-induced H_2 therapy could augment BTO-based SDT and enhance the tumor therapeutic efficacy by modulating the TME. Furthermore, BUM enhanced the efficacy of aPD-1 by modulating the immunosuppressive TME to an immunostimulatory TME.

1. Introduction

SDT represents an emerging non-invasive treatment modality that employs low-frequency, low-intensity US to stimulate sonosensitizers, thereby eradicating tumor cells. Compared to other exogenous stimuli such as light, temperature, and electricity, ultrasound as an exogenous energy has become a prominent area of research in the field of nanomedicine due to its noninvasiveness, tissue penetration depth (>10 cm), and minimal side effects.[2–4] It catalyzes sonosensitizers to generate cytotoxic reactive oxygen species (ROS) in tumor cells, which achieve antitumor effects by oxidizing lipids, destroying proteins, and damaging DNA.[5] However, due to the distinctive attributes of the TME (low pH, hypoxia),[6,7] the sustained production of ROS is significantly constrained, leading to a restricted therapeutic efficacy.[8] Additionally, despite the development of numerous sonosensitizers with enhanced performance over the past decade, there remains scope for further improvement in their therapeutic efficacy.[9,10] Thus, the combination of these sensitizers with other therapeutic modalities, such as those that amplify tumor oxidative stress and modulate the TME to activate tumor immunity,[11–14] may prove to be an

[a] Beijing Institute of Nanoenergy and Nanosystems, Chinese Academy of Sciences, Beijing 101400, China
[b] Tsinghua Changgung Hospital, School of Clinical Medicine, Tsinghua University, Beijing 100084, China. E-mail: li_zhou@tsinghua.edu.cn
[c] School of Biomedical Engineering, Tsinghua University, Beijing 100084, China
[d] School of Nanoscience and Engineering, University of Chinese Academy of Sciences, Beijing 100049, China. E-mail: xulingling@ucas.ac.cn
[e] Institute of Integrative Medicine, Department of Integrated Traditional Chinese and Western Medicine, Xiangya Hospital Central South University, Changsha 410008, China

† Electronic supplementary information (ESI) available. See DOI: https://doi.org/10.1039/d5mh00585j

effective means of enhancing the therapeutic efficacy of tumor treatment.

As an endogenous gas, H_2 has gained considerable attention in recent years due to its remarkable safety profile, high diffusibility, and regulatory roles in various pathological processes.[15–17] Over the past few decades, H_2 has demonstrated promising therapeutic effects in the treatment of a wide range of diseases, including tumors,[1,17–21] wound healing,[22,23] atherosclerosis,[24] acute ischemic stroke,[25] Alzheimer's disease[26] and arthritis.[27] Although the exact mechanism underlying the antitumor effects of H_2 remains unclear, its therapeutic efficacy is closely associated with the location of the lesion, duration of exposure, and concentration of H_2. Studies have shown that low concentrations of H_2 can specifically scavenge highly toxic hydroxyl radicals ($^{\bullet}OH$) and peroxynitrite ($ONOO^-$) in cells while preserving the physiological functions of other ROS in normal cells.[28,29] This makes it more suitable for the treatment of inflammation-related diseases,[30] with limited effects on cancer therapy. Conversely, high concentrations of H_2 can inhibit mitochondrial energy metabolism in cancer cells[18,31] and disrupt intracellular redox homeostasis, leading to an increase in ROS production,[15,32–34,36] which ultimately induces apoptosis of tumor cells and produces a more significant antitumor effect. Therefore, H_2 and ROS do not simply exhibit antagonistic actions in cells. The accumulation of ROS depends on the duration and concentration of H_2, as well as the state of the cell.[15,32–34,36] The common delivery methods for H_2 include inhalation of H_2-enriched air, injection of H_2-rich saline, and oral administration of H_2-rich water. However, due to its low solubility and small molecular size, these conventional delivery methods often struggle to achieve sufficiently high concentrations of H_2 at the tumor site, thus limiting their therapeutic effectiveness. Thus, to address this challenge, innov ative strategies have emerged, particularly involving the delivery of nanomaterials to tumor sites and utilizing endogenous or external stimuli to generate H_2 locally.[31,35] For example, palladium hydride ($PdH_{0.2}$) nanocrystals,[36] [FeFe]TPP/GEM/FCS nanocatalysts,[37] ammonia borane (AB),[21,38] nano CaH_2[18] and nanomaterials such as $PtBi_2S_3$ have been employed to achieve *in situ* H_2 release, thereby improving the H_2 delivery efficiency and exhibiting significant antitumor effects.[17,39,40] Nevertheless, despite the potential of H_2 therapy, standalone H_2 therapy still faces limitations in achieving optimal therapeutic outcomes. Consequently, combining SDT with H_2 therapy can offer a more precise, effective, and less toxic approach for tumor treatment. However, effectively integrating H_2 therapy with SDT to achieve a better anticancer outcome remains a critical challenge. MgH_2 is a solid H_2 source with high storage capacity[41] and the ability to be hydrolyzed to produce the desired H_2. Also, its byproduct $Mg(OH)_2$ can neutralize the acidic TME, and Mg^{2+} has been demonstrated to play a significant role in the immune response.[42] Therefore, MgH_2 has emerged as a promising candidate for cancer therapy and warrants further investigation and application.

Herein, we propose the use of MgH_2 as a new therapeutic agent for tumor treatment, through its synergistic combination with SDT. Firstly, MgH_2 nanoparticles were obtained *via* the liquid-phase exfoliation method. Then, they were prepared into MgH_2-PCL microspheres through electrospraying[43,44] to achieve the slow release of H_2 locally in tumors. BTO nanoparticles were prepared *via* the hydrothermal method. Then, the MgH_2-PCL microspheres and BTO nanoparticles were delivered into the CT26 tumor site. BTO-mediated SDT could directly kill tumor cells. The MgH_2 encapsulated in the microspheres could react with water to produce H_2, OH^- and Mg^{2+} at the tumor site. The generated H_2 further promoted tumor cell apoptosis by inducing mitochondrial dysfunction in tumor cells, while the OH^- could relieve the acidic microenvironment.[7] Therefore, more immune cells infiltrated the tumor site, and the tumor immunosuppressive microenvironment was improved. Furthermore, Mg^{2+} could recruit more $CD8^+$ T cells and the use of aPD-1 enhanced the T cell cytotoxicity to achieve a better therapeutic effect. Thus, MgH_2-induced H_2 therapy not only enhanced the effectiveness of tumor treatment and achieved H_2 therapy, but also realized the neutralization of the acidic TME and regulation of the immunosuppressive microenvironment. The synergistic effect of SDT and H_2 therapy greatly enhanced the effectiveness of tumor treatment. In addition, the efficacy of the immune checkpoint inhibitor (aPD-1) was enhanced due to the improvement of the TME (Fig. 1).

2. Results and discussion

2.1 Synthesis and characterization of BTO nanoparticles and MgH_2-PCL microspheres

BTO nanoparticles were synthesized through a hydrothermal method, as previously described.[45] Transmission electron microscopy (TEM) revealed that the BTO nanoparticles exhibited a tetragonal shape (Fig. 2(a)) with a diameter of 12 ± 2 nm (Fig. S1a, ESI†). The high-resolution TEM image further demonstrated an interplanar spacing of 0.28 nm, corresponding to the (110) plane of BTO (Fig. 2(b)). Additionally, the X-ray diffraction (XRD) pattern of BTO showed separated (002) and (200) reflections, consistent with the characteristic of tetragonal piezoelectric BTO (Fig. 2(c)).[5] Fourier transform infrared spectroscopy (FTIR) spectroscopy showed that BTO exhibited absorption bands at around 550 cm^{-1} and the MgH_2 exhibited absorption bands at around 450–500 cm^{-1}, as shown in Fig. S2a (ESI†). Raman spectroscopy identified a prominent A_1(2TO) signal at 247 cm^{-1} and the E(3TO) + E(2LO) + B_1 signal at 307 cm^{-1} (Fig. S2b, ESI†), which are characteristic Raman scattering modes of tetragonal BTO, further supporting the tetragonal structure of BTO. Fig. S2d (ESI†) shows four major peaks, which were assigned to C 1s, Ti 2p, O 1s, and Ba 3d, respectively. The peaks at 458 eV and 463.9 eV correspond to Ti $2p_{3/2}$ and Ti $2p_{1/2}$, respectively. Ba $3d_{3/2}$ (794.4 eV) and Ba $3d_{5/2}$ (779.0 eV) of BTO were detected in the Ba 3d spectrum of BTO. The peaks at 529.5 eV and 531.2 eV, corresponding to lattice oxygen and oxygen vacancies, respectively, were separated from the asymmetric O 1s spectrum, confirming the presence of oxygen vacancies, as shown in Fig. S2e (ESI†).[45]

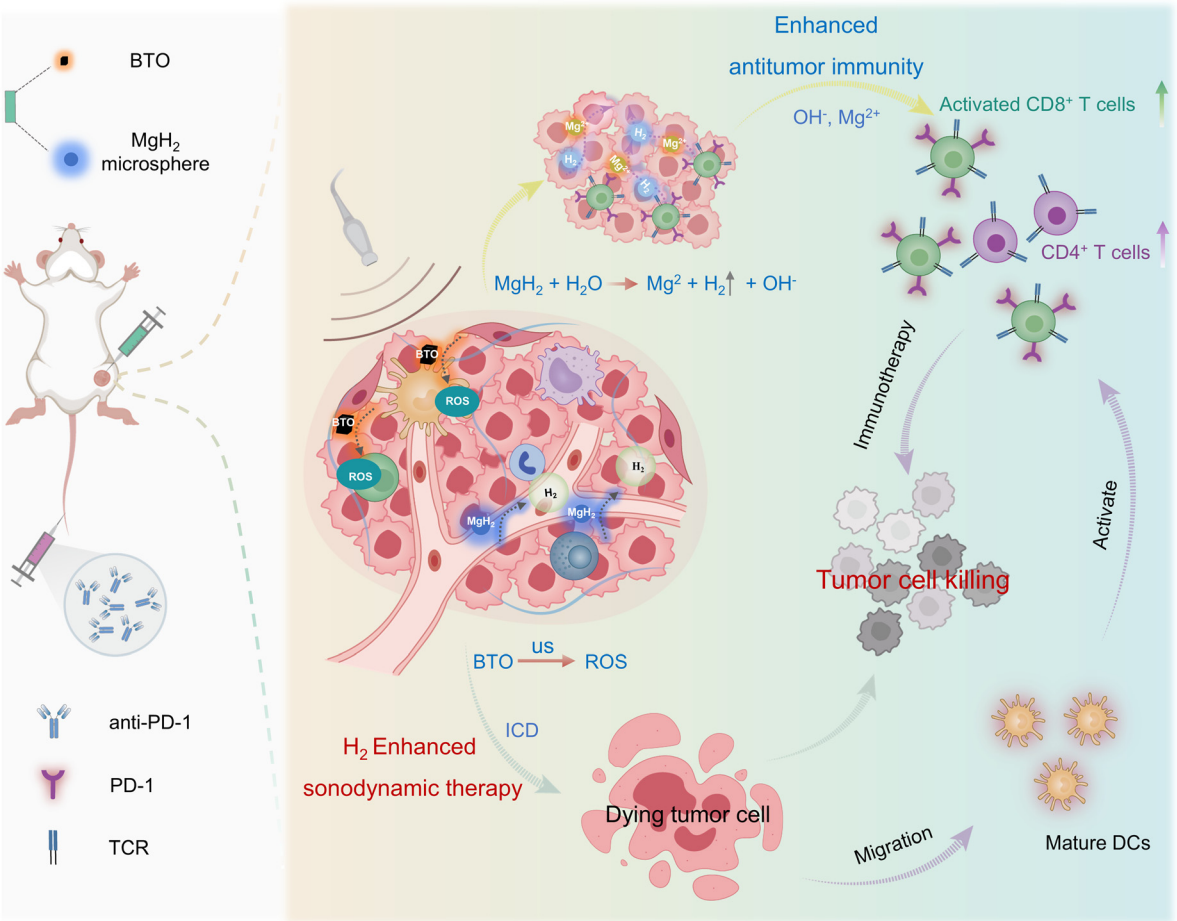

Fig. 1 Schematic of the *in situ* H_2 therapy induced by MgH_2, potentiating SDT through disruption of redox homeostasis in tumor cells and regulation of the TME (TCR: T cell receptor).

The piezoelectric catalytic activity of BTO under ultrasonic stimulation was confirmed by a methylene blue (MB) degradation assay, and the results are presented in Fig. 2(d). With the extension of the US application time, the absorbance of the MB solution containing BTO nanoparticles at 664 nm gradually decreased, indicating a corresponding increase in ROS production. Furthermore, ESR (electron spin resonance) spectroscopy with DMPO spin-trapping confirmed the generation of hydroxyl radicals ($^{\bullet}OH$) during dye degradation (Fig. 2(e)). The BTO + US group exhibited stronger DMPO–$^{\bullet}OH$ adduct signals compared to the US-only and BTO-only groups, demonstrating the synergistic catalytic activity of BTO nanoparticles.

The MgH_2 nanoparticles were synthesized using a liquid-phase exfoliation method[18,46,47] (Fig. 2(g)). According to the scanning electron microscopy (SEM) images, the micron MgH_2 powder was successfully exfoliated into small nanoparticles with a size of 122 ± 54 nm (Fig. S1b–d, ESI†). The characteristic XRD peaks corresponded to the lattice surface of MgH_2, confirming that the polycrystals belong to MgH_2 (PDF#12-0697) (Fig. 2(c)). To control H_2 release, MgH_2 microspheres were prepared using the electrospray technique after blending the MgH_2 nanoparticles with PCL solution (Fig. 2(g)). By modifying the voltage, the concentration of the PCL solution, and the spray distance, uniform microspheres with a diameter of approximately 5 μm were obtained (Fig. S3, ESI†). SEM showed that the microspheres exhibited a uniform spherical morphology, while elemental mapping demonstrated that C and Mg were distributed uniformly within the microspheres, confirming the homogeneous distribution of MgH_2 within the microspheres (Fig. 2(h)). To better observe the release of H_2 from MgH_2, MgH_2-PCL tablets were prepared and placed in PBS for observation. Under an optical microscope, the continuous generation of H_2 bubbles was observed on the surface of the tablets (Fig. 2(i)).

Methylene blue–platinum (MB–Pt) was used as a probe to further confirm that the gas released by the microspheres was H_2. As shown in Fig. 2(f), the absorbance of the blue MB decreased over time, given that the H_2 generated by MgH_2 facilitated the reduction of the blue MB to the colorless leucomethylene blue (LMB) in the presence of the Pt catalyst. Following exposure to air in the same reaction system, the colorless LMB was rapidly converted back to MB by oxygen oxidation (Fig. 2(j)).[48] Subsequently, the quantitative measurement of H_2 release from the MgH_2 microspheres was conducted

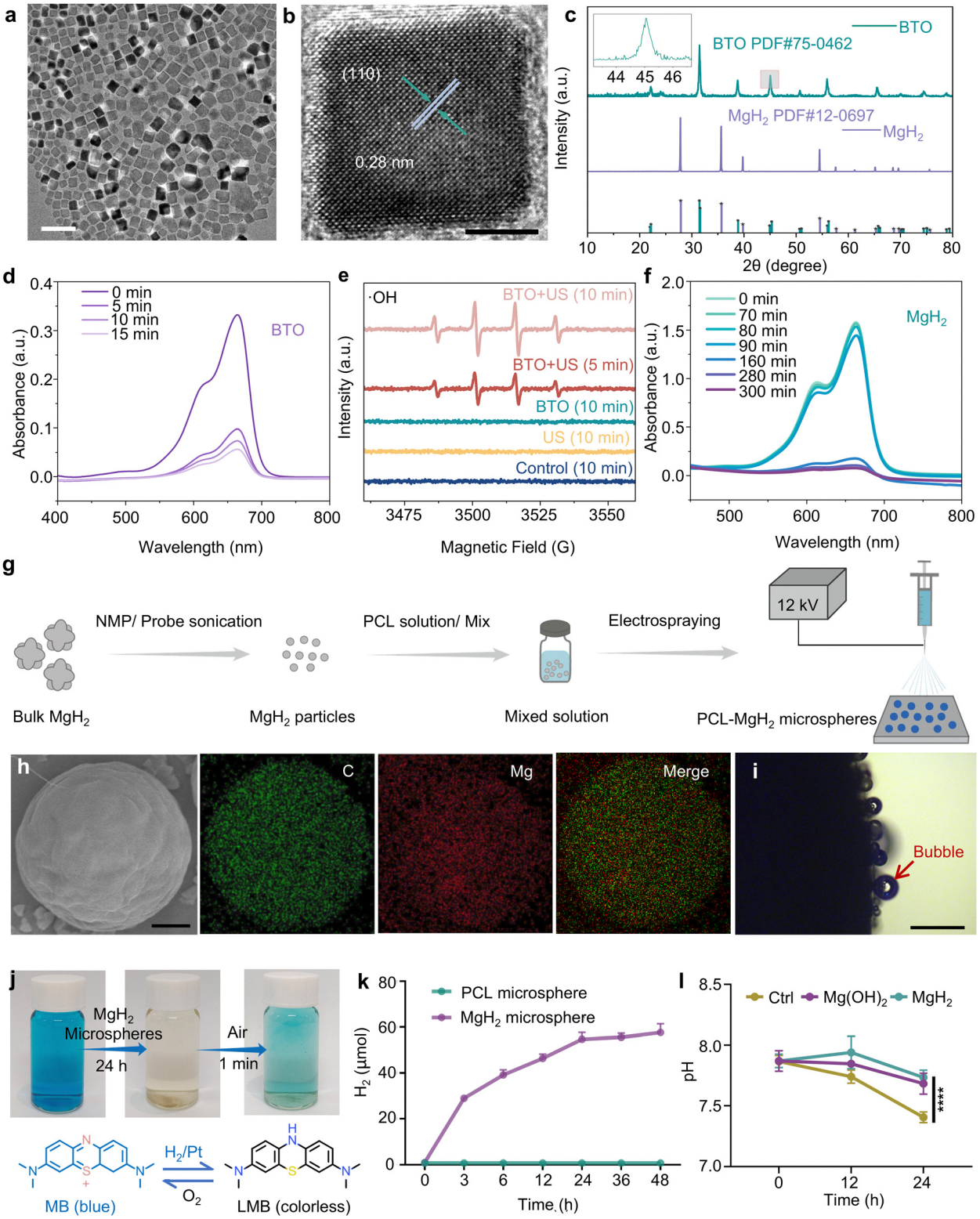

Fig. 2 Characterization of BTO nanoparticles and MgH_2 microspheres. (a) TEM image (scale bar = 50 nm) and (b) high-resolution transmission electron microscopy (HRTEM) image of BTO nanoparticles (scale bar = 5 nm). (c) XRD pattern of BTO nanoparticles (insert image of the enlarged (002 and 200) peaks) and MgH_2 particles. (d) UV-vis absorbance spectra of MB under US irradiation (1.0 MHz, 1.0 W cm^{-2}, 50% duty cycle) in the presence of BTO nanoparticles. (e) ESR spectra of •OH trapped by DMPO under different experimental conditions. (f) UV-vis absorbance spectra of MB–Pt after reduction of MB by H_2 generated by MgH_2 at different time points. (g) Process for the preparation of PCL-MgH_2 microspheres (it was shortened to MgH_2 microspheres in the latest article). (h) SEM images and elemental mapping of MgH_2 microspheres (scale bar = 1 μm). (i) Photograph of bubbles generated on the surface of a PCL tablet containing MgH_2 in it. (The bubbles on the surface of the tablet could be easily observed compared with MgH_2 microspheres, scale bar = 500 μm.) (j) Photograph showing reversible disappearance of the blue color of the MB–Pt probe (10 μg mL^{-1} MB + 60 μg mL^{-1} Pt) after H_2 reduction and air contact. (k) Released H_2 in ×1 PBS measured by gas chromatography (GC). (l) pH value changes of the buffer in the presence of $Mg(OH)_2$ microspheres and MgH_2 microspheres measured by pH microelectrode.

by gas chromatography. As illustrated in Fig. 2(k), the MgH_2 microspheres were capable of releasing H_2 for up to 48 h in PBS. Following the co-incubation of MgH_2 with tumor cells, the pH of the culture medium in the MgH_2 group was significantly higher than that of the Ctrl group, which is likely due to the reaction between MgH_2 and H_2O to form $Mg(OH)_2$, indicating the potential of MgH_2 to modulate the acidic TME (Fig. 2(l)).

2.2 Evaluation of synergistic anti-tumor effects *in vitro*

To determine the impact of individual BTO and MgH_2 microspheres on normal cells, a Cell Counting Kit 8 (CCK8) experiment was conducted. The results showed that in the case of normal human immortalized keratinocytes (HaCat), at BTO concentrations of up to 500 μg mL^{-1} and MgH_2 concentrations of up to 400 μg mL^{-1}, the cell viability was not significantly affected (Fig. S4a and b, ESI†). To investigate the killing effect of BTO and MgH_2 microspheres on tumor cells under the effect of US, we firstly incubated the materials with the cells for 4 h, and then after H_2 exerted its effect, we carried out US intervention to achieve synergistic treatment. In melanoma B16F10 cells, the antitumor effect of BTO under US stimulation showed a dose-dependent enhancement, where at a BTO concentration of 100 μg mL^{-1}, the cell survival rate was 70%, and it further decreased to 31% at 500 μg mL^{-1}. When 300 μg mL^{-1} MgH_2 was added to 100 μg mL^{-1} BTO solution, the cell survival rate remained above 90%, consistent with the results for BTO alone, indicating that the combination of these two materials alone did not enhance the antitumor effect. However, when US was applied, the cell viability significantly decreased to 60%, which was lower than that of the BTO + US group, suggesting that MgH_2 enhanced the sonodynamic therapeutic effect triggered by US (Fig. 3(a) and Fig. S5a, b, ESI†). In the case of 4T1 and CT26 cells, as shown in Fig. 3(b) and (c), respectively, the combination of BTO + MgH_2 under US stimulation also exhibited the most significant tumor inhibition, suggesting its synergistic anti-tumor effect in different tumor cells.

To further demonstrate the synergistic antitumor efficacy of BTO + MgH_2, live–dead staining was performed on B16F10 cells subjected to different treatments (Fig. 3(d) and Fig. S7c, d, ESI†). The results showed that the BTO + US + MgH_2 (BUM) group exhibited the strongest red fluorescence intensity, indicating its highest efficiency for tumor cell elimination. It has been demonstrated that BTO induces apoptosis by generating ROS in the presence of US.[5,8] Thus, to investigate ROS production under various conditions, we analyzed B16F10 cells using DCFH-DA staining (Fig. 3(e) and Fig. S7a, b, ESI†). Minimal green fluorescence was observed in the Ctrl, BTO, BTO + MgH_2, and US-only groups, indicating negligible ROS generation. In contrast, the BTO + US group exhibited noticeable green fluorescence, which was further enhanced with the addition of MgH_2, indicating a significant increase in ROS levels. The elevated ROS may be related to the disruption of redox homeostasis in the tumor cells, leading to oxidative stress in the cells. Tumor cells are more sensitive to H_2 than normal cells because they have higher ROS. Compared to normal cells, cancer cells exhibit greater suppression of redox stress.[36] Initially, H_2 selectively reduces the intracellular ROS levels upon entry into tumor cells; however, a rebound in the elevation of ROS occurs due to the redox homeostatic capacity of the cell.[12,31–36] Subsequent BTO-mediated SDT exacerbates oxidative stress in tumor cells, leading to the significant elevation of ROS within tumor cells.

Considering the close correlation between ROS and mitochondrial function,[32] as well as the pivotal importance of the mitochondrial membrane potential (MMP) in maintaining the mitochondrial integrity, we employed the JC-10 probe to assess the alterations in mitochondrial membrane potential (Fig. 3(f) and (j)). Under the conditions of a high mitochondrial membrane potential, as observed in the Ctrl group, JC-10 aggregated to form polymers, emitting red fluorescence. Conversely, a reduction in the mitochondrial membrane potential led to the dissociation of JC-10 into monomers, resulting in green fluorescence emission. Among the treatment groups, the BUM group exhibited the most intense green fluorescence, indicating a substantial decrease in mitochondrial membrane potential, a hallmark event in the early stages of apoptosis. Statistical analysis of the mitochondrial membrane potential revealed a significantly higher monomer/aggregate fluorescence intensity ratio in the BUM group compared to the Ctrl, MgH_2 and BTO + US groups, indicating BUM-induced mitochondrial membrane potential depolarization to trigger apoptotic cell death. Green fluorescence was also observed in the MgH_2 group, suggesting that H_2 produced by MgH_2 can cause damage to mitochondria by inhibiting mitochondrial function.[49] Subsequently, the apoptosis rate of each group after 24 h of treatment was quantified by Annexin V-APC/PI staining (Fig. 3(g)–(i)). The results demonstrated that the control group exhibited negligible levels of apoptosis. Treatment with BTO + US induced a noticeable increase in both early (32.87%) and late apoptosis (9.97%), whereas the MgH_2 group showed a similar level of early apoptosis as the BTO group (33.17%) but with negligible late apoptosis (3.23%). In contrast, the BUM group displayed the highest levels of both early and late apoptosis (54.9% and 18.8%, respectively), with the total apoptosis rate reaching 73%. The large reduction in MMP and high apoptosis rate in the BUM group were associated with the high amount of ROS generated in the tumor cells due to H_2 synergistic SDT. These findings indicate that the combined application of BTO + US and MgH_2 significantly enhanced tumor cell apoptosis, highlighting the synergistic effect of the combined treatment.

The hallmarks of immunogenic cell death (ICD) primarily include the release of adenosine triphosphate (ATP) from dying cells, pre-apoptotic exposure of calreticulin (CRT) on the cell surface, and post-mortem release of high mobility group box 1 (HMGB1) into the extracellular space.[50] HMGB1 release and CRT exposure were observed through CLSM (Fig. 3(k) and (l)). The lowest red fluorescence intensity was observed in the BUM group, indicating the significant release of HMGB1, as shown in Fig. 3(k). At the same time, the highest extranuclear red fluorescence intensity was observed in this group, showing the most CRT exposure (Fig. 3(l)). Also, we detected the ATP

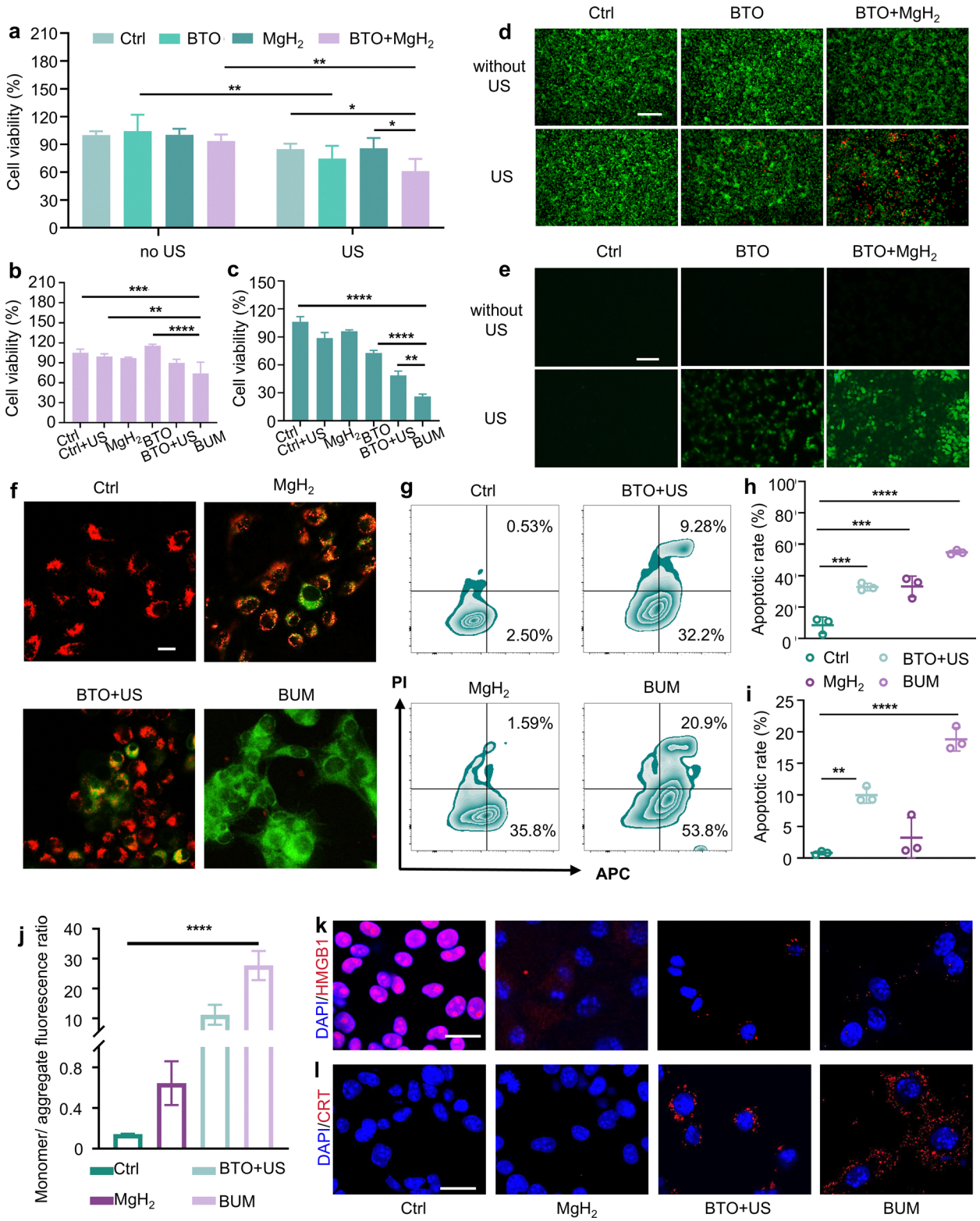

Fig. 3 *In vitro* therapy efficacies of BTO nanoparticles and MgH_2 microspheres. Relative viabilities of (a) B16F10 cells, (b) 4T1 cells and (c) CT26 cells after incubation under various conditions (BTO: 100 μg mL^{-1}; MgH_2: 300 μg mL^{-1}; US irradiation: 1 W cm^{-2}, 5 min; n = 4). (d) Calcein-AM/PI fluorescence images of B16F10 cells after different treatments. Live cells (green) and dead cells (red) detected by Calcein-AM/PI staining, respectively (scale bar: 200 μm). (e) Levels of ROS in B16F10 cells after different treatments detected by DCFH-DA staining (scale bar = 100 μm). (f) Confocal fluorescence images of mitochondria membrane potential in B16F10 cells after different treatments (BTO: 100 μg mL^{-1}; MgH_2: 300 μg mL^{-1}; US irradiation: 1 W cm^{-2}, 5 min; scale bar = 15 μm). (g) Flow cytometric analysis of apoptosis in B16F10 cells with various treatments. Statistical analysis of (h) early apoptotic rate and (i) late apoptotic rate of B16F10 cells with various treatments (n = 3). (j) Statistical analysis of mitochondrial membrane potential. Fluorescence images of ICD markers (k) HMGB1 and (l) CRT in B16F10 cells after different treatments. Scale bar = 25 μm. Data are represented as mean ± SD in (a, b, c, h, and i). *P < 0.05, **P < 0.01, and ***P < 0.001.

content. According to Fig. S6 (ESI†), the lowest ATP content can clearly be observed in the tumor cells in the BUM group, which indicated the most secretion of ATP in BUM group. All of the above-mentioned results demonstrated that BUM could lead to ICD, which is beneficial for the regulation of TME.

2.3 *In vivo* combined tumor therapy

The therapeutic efficacy of BUM was evaluated in subcutaneous CT26 tumor-bearing mice, with the complete treatment process illustrated in Fig. 4(a). The mice were divided into four groups including Ctrl, MgH_2, BTO + US and BUM, each subjected to different treatments over the first 6 days. As shown in Fig. 4(b) and (c), the tumors in the MgH_2, BTO + US and BUM groups grew slower than that in the Ctrl group, with the BUM group showing the slowest growth, significantly demonstrating the strongest inhibitory effect on tumor progression. On the fourteenth day after treatment, the average tumor volume was 1102 mm^3 in the Ctrl group, 632 mm^3 in the MgH_2 group, and 489 mm^3 in the BTO + US group, whereas the average tumor volume in the BUM group was only 235 mm^3. Statistical analysis revealed that the tumor volume in the BUM group was significantly reduced compared to the Ctrl group ($P < 0.001$). This indicates that the synergistic treatment of SDT and H_2 has a stronger inhibitory effect on tumor growth than that of the single treatment. Additionally, the tumors in the BUM group also exhibited the lowest weight with a mean mass of only 167.6 mg (Fig. 4(e)) and the smallest size (Fig. 4(f) and Fig. S5, ESI†), further highlighting its superior treatment efficacy. The combined effect of piezoelectric catalysis and H_2 showed a significant ability to inhibit tumor growth.

Furthermore, to accurately determine the extent of H_2 production within the tumor, it was observed by ultrasound imaging. Following the injection of MgH_2 microspheres into the tumor, the bright echoes were observed, which corresponded to the H_2 bubbles generated by MgH_2 microspheres, exhibiting strong contrast under ultrasound imaging. As shown in Fig. 4(g), the bright echoes persisted for more than 24 h, indicating that MgH_2 microspheres can continuously release H_2 at the tumor site.[51] Notably, this H_2 vesicle may also destroy the tumor in the presence of ultrasound irradiation.[33]

To further validate the therapeutic outcomes, we employed hematoxylin–eosin staining (H&E), terminal deoxynucleotidyl transferase-mediated dUTP nick-end labelling (TUNEL), and ki67 to assess the pathological state of the tumor tissues following different treatments, as shown in Fig. 4(h). H&E staining revealed a marked reduction in nuclei in the BUM group, with severe nuclear shrinkage and division, indicating typical histopathological damage. Concurrently, TUNEL staining demonstrated the most intense green fluorescence in this group, indicating the highest level of tumor cell apoptosis. The results of ki67 staining demonstrated that nuclei with brown deposits were most abundant in the Ctrl group and least abundant in the BUM group, indicating high cell proliferation in the Ctrl group, in contrast to the minimal proliferation observed in the BUM group, thereby confirming the effective tumor growth inhibition achieved with this treatment.

To investigate the pro-inflammatory effects of BUM, at the cellular level, RAW 264.7 cells and bone marrow-derived macrophages were co-cultured with supernatants from the differently treated B16F10 cells. As shown in Fig. S8 (ESI†), the expression levels of pro-inflammatory cytokines IL-1β, IL-6, and TNF-α were highest in the BUM group, indicating that BUM induced ICD in the tumor cells, thereby enhancing the pro-inflammatory response of macrophages.

The release of pro-inflammatory factors at the tumor site after the different treatments was detected. Fig. 4(i)–(k) show that the BUM group exhibited the highest levels of TNF-α, IL-1β, and IL-6, consistent with the cellular findings. Notably, the IL-6 content in the BUM group was twice that of the MgH_2 and BTO + US groups.

A comprehensive and systematic biosafety assessment of the materials was conducted throughout the treatment period. Throughout the treatment period, the body weights of the mice in both the experimental and control groups remained stable, showing no significant changes (Fig. 4(d)). Blood samples were collected to analyze a range of hematological parameters, including mean corpuscular hemoglobin [MCH], platelets [PLT], red blood cells [RBC], basophils [BA], eosinophilic granulocytes [EO], monocytes [MO], hemoglobin [HGB], lymphocytes [LY], neutrophilic granulocytes [NE], hematocrit [HCT], standard deviation of red blood cell distribution width [RDW-SD], platelet distribution width [PDW], mean corpuscular volume [MCV] and mean platelet volume [MPV] (Fig. S10, ESI†). The results indicated no statistically significant differences in these hematological indices across the treatment groups, with only minor fluctuations within the expected physiological ranges. Furthermore, H&E staining of the major organs in the experimental groups showed no significant tissue damage among the treatment groups (Fig. S12, ESI†), confirming the favorable biological safety profile of the treatment regimen.

2.4 *In vivo* immune response

Tumor-associated macrophages (TAMs) are macrophages infiltrated in tumor tissues with diverse phenotypic activation depending on the TME. M1 TAMs are known to kill tumor cells and defend against pathogens, while M2 TAMs mainly promote tumor growth, invasion, and metastasis. The acidic TME impedes anti-tumor immunity by inhibiting the M1 polarization of macrophages, promoting their shift toward the immunosuppressive M2 phenotype, and suppressing T cell proliferation and cytotoxic functions. Neutralizing tumor acidity and introducing H_2 has been shown to modulate the immunosuppressive characteristics of the TME, thereby enhancing the anti-tumor immunity.[18,52]

Considering this, we investigated the effects of H_2 synergistic piezoelectric catalysis on the immune microenvironment and anti-tumor immunity in CT26-bearing mice. The mice were sacrificed on day 7 after treatment, and tumor tissues were collected for flow cytometry to measure the percentage of immune cells. The phenotypes of TAMs in the TME were further characterized. As shown in Fig. 5(a)–(c), the Ctrl group predominantly exhibited M2-type macrophages, indicating an

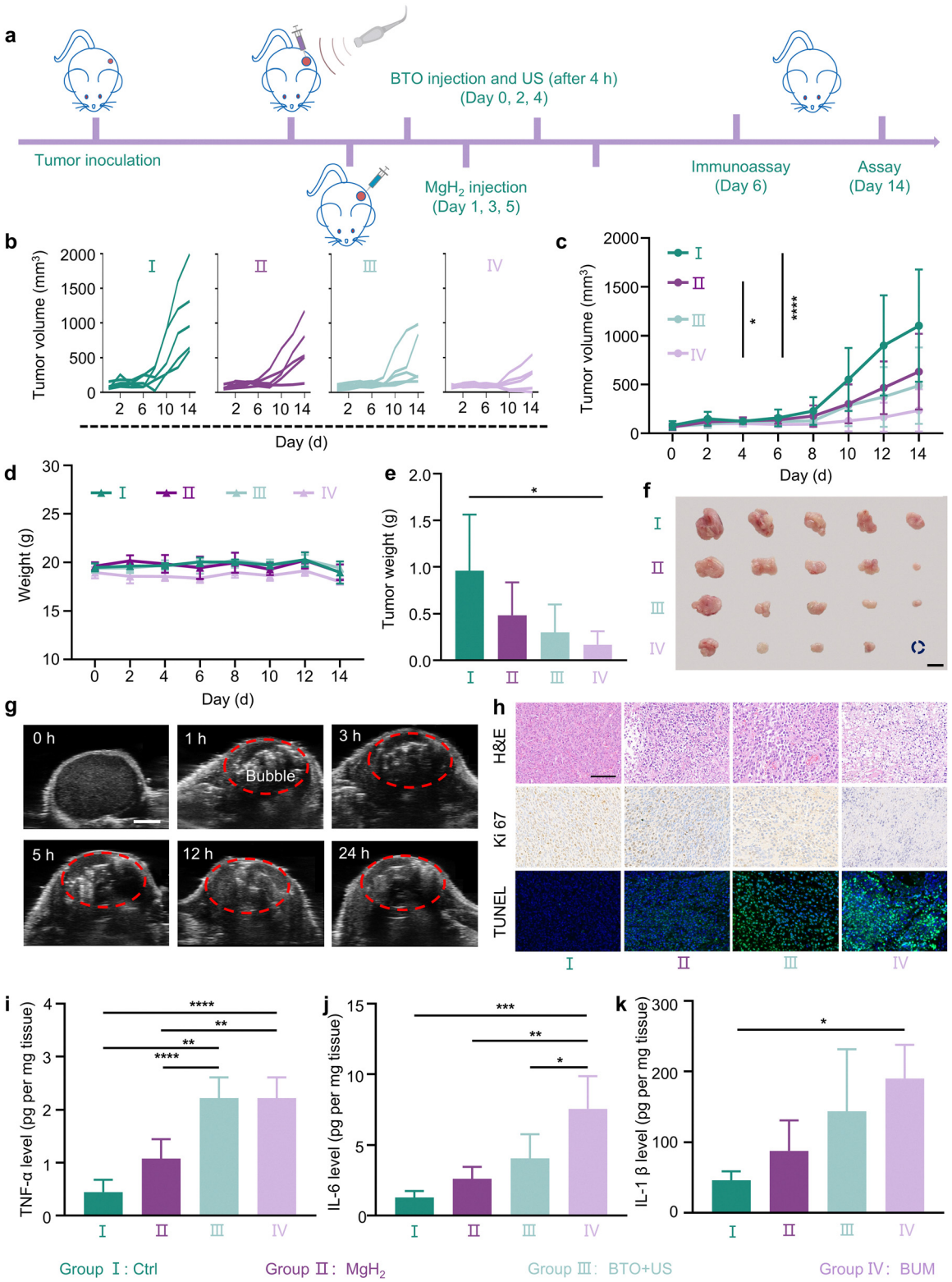

Fig. 4 *In vivo* combined therapy (n = 5). (a) Schematic of the cancer therapeutic process. (b) Individual time-dependent tumor growth curves (c) and time-dependent tumor growth curves of CT26 tumor-bearing mice after different treatments, including control group, MgH_2 group, BTO + US group and BTO + US + MgH_2 group (BTO: 10 mg kg^{-1}; MgH_2 microspheres: 130 μg per mouse; US irradiation: 1 W cm^{-2}, 8 min). (d) Time-dependent body-weight curves and (e) tumor weight of CT26 tumor-bearing mice after different treatments. (f) Digital images of tumors collected from CT26 tumor-bearing mice at the end of the antitumor studies (scale bar = 1 cm). (g) Ultrasonic imaging of CT26 tumor-bearing mice after injection of MgH_2 microspheres (the enhanced signal intensities indicate generated H_2 bubbles, scale bar = 2 mm). (h) Microscopy images of H&E, TUNEL and ki67 stained tumor slices collected from mice after different treatments (scale bar = 100 μm). (i) TNF-α, (j) IL-6, and (k) IL-1β levels at tumor sites after different treatments. Data are represented as mean ± SD in (a, b, c, h, and i). *$P < 0.05$, **$P < 0.01$, and ***$P < 0.001$.

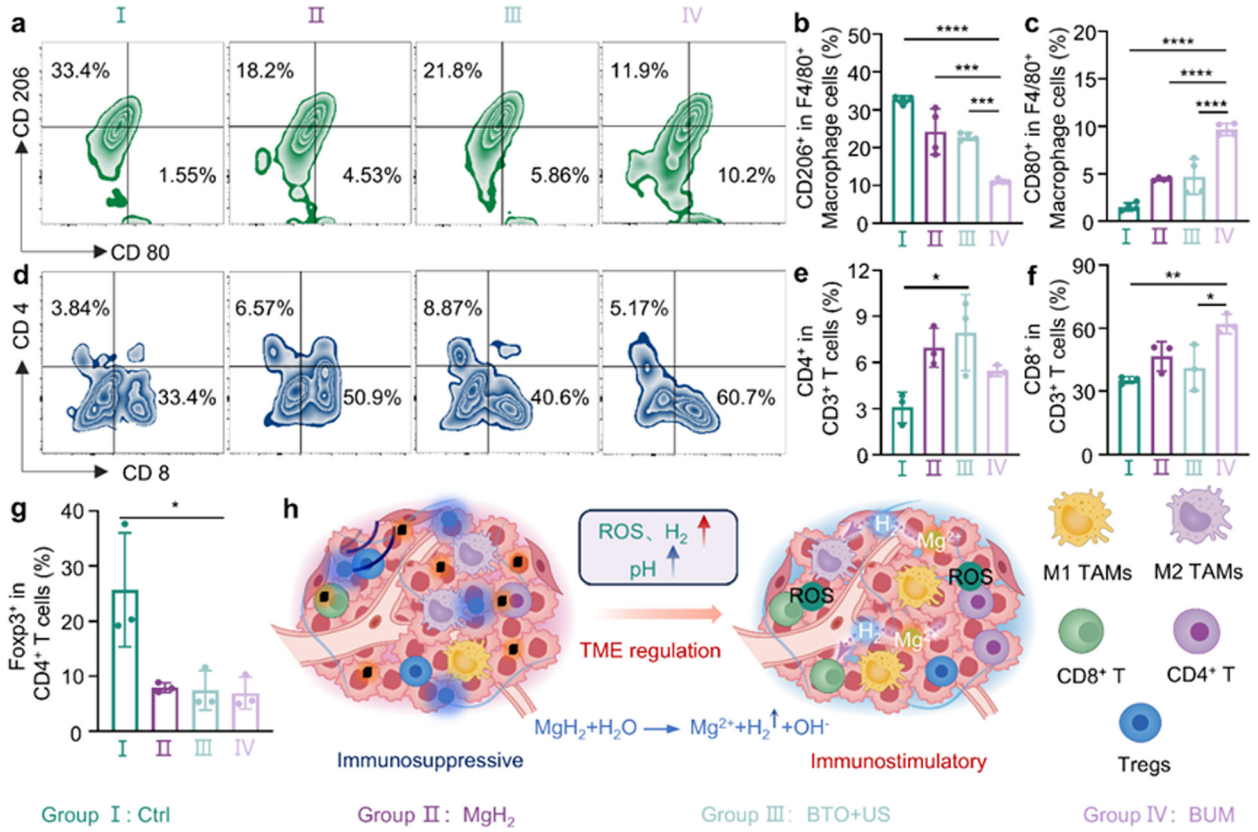

Fig. 5 *In vivo* immune responses. (a) Flow cytometric analysis results and (b) and (c) quantification results of M1-type macrophages ($CD11b^+F4/80^+CD80^+$) and M2-type macrophages ($CD11b^+F4/80^+CD206^+$) within the tumors after different treatments (n = 4). (d) Flow cytometric analysis results and (e) and (f) quantification results of $CD4^+$ T cells ($CD45^+CD3^+CD4^+$) and $CD8^+$ T cells ($CD45^+CD3^+CD8^+$) within the tumors after different treatments (n = 3). (g) Quantification results of T_{regs} ($CD3^+CD4^+Foxp3^+$) within the tumors after different treatments (n = 3). (h) Schematic showing that BTO nanoparticles under US irradiation and H_2 generated from MgH_2 microspheres could activate the immune system. Data are represented as mean ± SD in (a, b, c, h, and i). *$P < 0.05$, **$P < 0.01$, and ***$P < 0.001$.

immunosuppressive TME. Treatment with MgH_2 or BTO + US alone effectively increased the proportion of M1 TAMs ($CD80^+$ in $F4/80^+$ macrophage cells), while reducing M2-type macrophages ($CD206^+$ in $F4/80^+$ macrophage cells), suggesting that these individual therapies can improve the tumor immune microenvironment. Notably, in the BUM group, the proportion of M1 TAMs was significantly higher than in the other groups, while the proportion of M2 TAMs were markedly lower. Further quantitative analyses confirmed that the changes in M1 and M2-type macrophages in the BUM group were significantly more pronounced compared to the single-treatment groups. These findings indicate that while individual treatments can effectively improve the tumor immune microenvironment, the combined application of MgH_2 and SDT exhibited a stronger synergistic effect, leading to the more substantial polarization of M2 TAMs into M1 TAMs, thereby more effectively enhancing the antitumor immune microenvironment.[20]

T cells play a crucial role in antitumor immunity by directly killing tumor cells or helping to activate other immune cells, thereby exerting a strong antitumor effect. Therefore, we further analyzed the changes in T cells in the different treatment groups to evaluate the impact of the treatments on tumor immune responses. Flow cytometry revealed that the tumor site in the BUM group exhibited a significantly higher number of T cells ($CD8^+$ T cells and $CD4^+$ T cells) compared to the Ctrl group and the MgH_2 group (Fig. 5(d)–(f)). Specifically, the percentage of $CD8^+$T cells was 1.5 times higher than in the control and BTO + US groups. This increase may be ascribed to two factors. Primarily, piezoelectric catalysis resulted in the generation of ROS, which induced ICD[8,53,54] and stimulated immune cell recruitment. Secondly, the generation of Mg^{2+} and OH^- from MgH_2 at the tumor site may reduce T cell inactivation by improving the microenvironment. Furthermore, the percentage of $CD4^+$ T cells in the lymph nodes of the BUM group was significantly higher than that of the other groups (Fig. S13, ESI†). This could enhance the anti-tumor immunity by directly killing tumor cells and activating $CD8^+$ T cells. In addition, the percentage of immunosuppressive regulatory T cells (T_{reg}) in the BUM group was lower than that in the control group (Fig. 5(g)), supporting the construction of an immunestimulatory microenvironment within the tumor. The abovementioned results indicated that MgH_2 and BTO + US could generate H_2, ROS and alkaline substances, which can activate macrophages and T cells and inhibit T_{reg} cells by regulating the

immunosuppressive TME into immune stimulation, thus achieving better immunotherapy effect (Fig. 5(h)).

2.5 Combined immune checkpoint blocking therapy (ICB)

It has been reported that Mg^{2+} can regulate the effector function of $CD8^+$ T cells and express higher levels of PD-1. Following the administration of $MgCl_2$ in conjunction with a-PD-1 inhibitor, the tumor progression in the mice was more effectively managed.[39] Considering that Mg^{2+} was released by MgH_2 during treatment, we also analyzed the expression of PD-1 receptor on the surface of T cells by flow analysis. As shown in Fig. 6(a) and (b), the expression of PD-1 on the surface of T cells in both the MgH_2 group and BUM group was nearly 10 times higher than that in the control group. Therefore, BUM was combined with a PD-1 inhibitor to treat CT26 tumor-bearing mice and observe its therapeutic effect. The experimental scheme is shown in Fig. 6(c).

To visually confirm the therapeutic effect, we used mice carrying subcutaneous CT26 tumors expressing firefly luciferase.

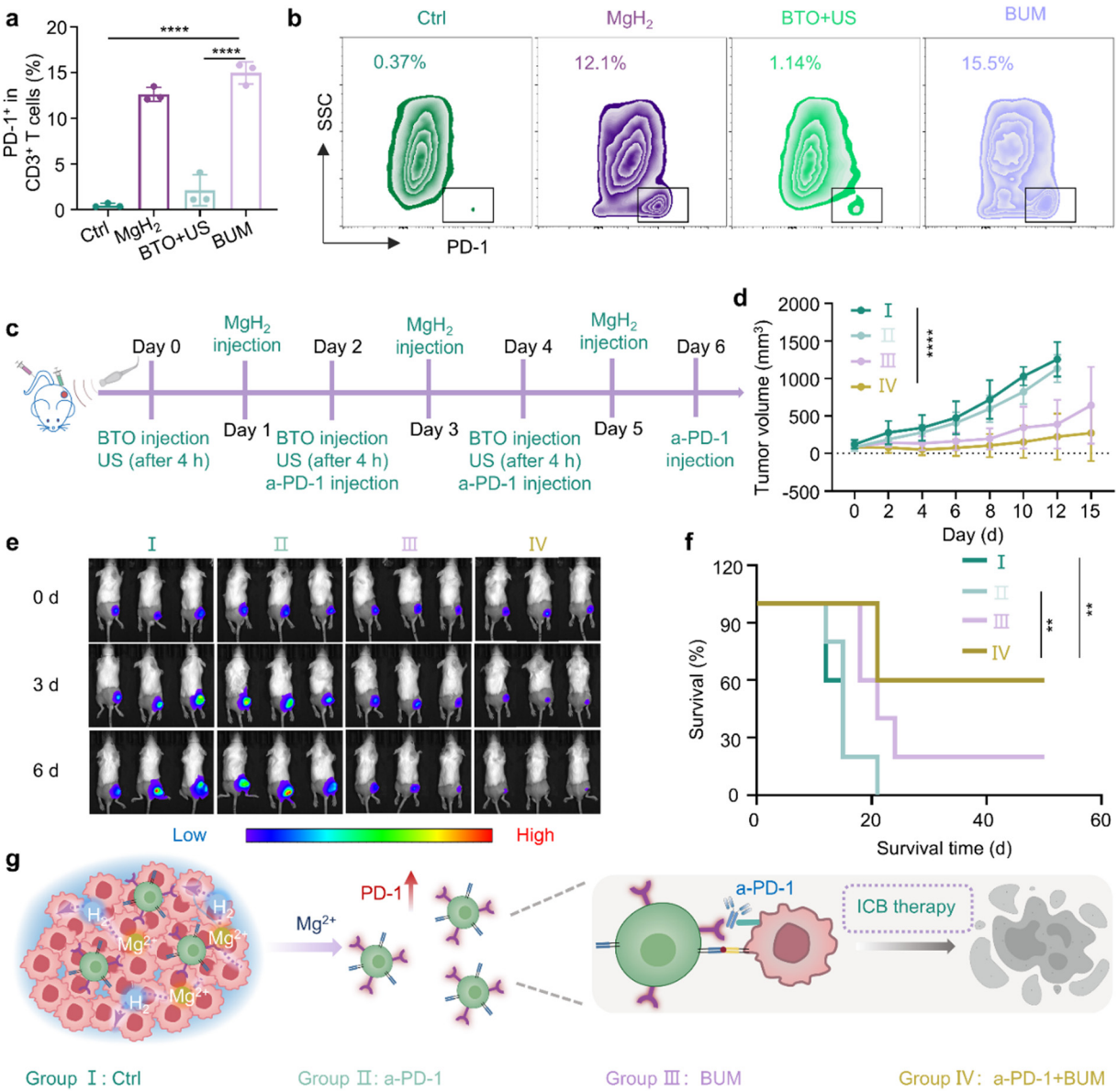

Fig. 6 Immunotherapy combined with a-PD-1. (a) Quantification results and (b) flow cytometric analysis results of $CD3^+$ T cells expressing PD-1 after different treatments (n = 3). (c) Schematic showing the therapeutic procedure of immunotherapy combined with a-PD-1 triggered by BTO nanoparticles and MgH_2 microspheres. (d) Time-dependent tumor growth curves of CT26 tumor-bearing mice after different treatments, including control group, a-PD-1 group, BUM group and a-PD-1 + BUM group (BTO: 10 mg kg^{-1}; MgH_2 microspheres: 130 μg per mouse; a-PD-1: 20 μg per mouse; US irradiation: 1 W cm^{-2}, 8 min; n = 5). (e) *In vivo* bioluminescence images of CT26 tumor-bearing mice expressing firefly luciferase after different treatments (n = 3). (f) Survival rates of tumor-bearing mice after various treatments after different treatments (n = 5). (g) Schematic of the mechanism of antitumor immune responses induced by BTO nanoparticles and MgH_2 microspheres in combination with a-PD-1. Data are represented as mean ± SD in (a, b, c, h, and i). *P < 0.05, **P < 0.01, and ***P < 0.001.

As seen in Fig. 6(d), the tumors in the a-PD-1 + BUM group exhibited the weakest fluorescence, indicating the most favorable treatment outcome in this group. In contrast, a-PD-1 monotherapy showed limited tumor inhibition, suggesting its weak efficacy when used alone. The tumor volume curves further highlighted the therapeutic potential of tumor therapy in the a-PD-1 + BUM group (Fig. 6(e)). It is worth noting that the survival time of the mice was significantly prolonged in both the BUM group and a-PD-1 + BUM group, with survival rates of 20% and 60%, respectively, at day 50 (Fig. 6(f)). These results demonstrate that BUM, in combination with immune checkpoint inhibitors, can further enhance the antitumor therapeutic outcomes, as shown in Fig. 6(g).

3. Conclusions

In summary, this study introduced a synergistic SDT/H_2 therapy strategy. Nano-scale MgH_2 was synthesized using liquid-phase exfoliation, while micron-sized microspheres were developed by combining PCL with the electrospray technique to achieve controlled H_2 release. This approach, as a novel anticancer agent, disrupts mitochondrial function, and in combination with BTO-mediated SDT, greatly amplifies the therapeutic effectiveness.

A key innovation of this approach addresses the limitations of conventional SDT, which is often hindered by the TME due to its acidic pH. The OH^- produced by the reaction of MgH_2 microspheres with water can neutralize the acidic TME, creating a more favorable therapeutic environment. Meanwhile, the produced H_2 can be synergistic with SDT to promote oxidative stress in tumor cells, thereby inducing significant tumor cell apoptosis. In addition to directly affecting tumor cells, the synergistic effect of MgH_2-induced H_2 therapy and SDT significantly increased immune cell infiltration and attenuated immunosuppression. This effect is evident in the increased presence of $CD8^+$ and $CD4^+$ T cells, the polarization of M2-type TAMs towards the M1 phenotype, and a reduction in Treg cells. Furthermore, the release of Mg^{2+} ions activated $CD8^+$ T cells and strengthened the anti-tumor immunity. The *in vivo* studies on tumor-bearing mice demonstrated that this combination therapy effectively inhibited tumor growth. Additionally, this synergistic approach can enhance the efficacy of ICB therapy, achieving improved therapeutic outcomes. Furthermore, it is important to highlight that the degradation products of MgH_2 (Mg^{2+}, OH^-, and H_2), along with the FDA-approved biodegradable PCL, do not induce any adverse effects on the body. Thus, due to their broad applicability, MgH_2 microspheres can serve as a versatile platform for synergistic combination therapies, such as immune checkpoint inhibition, radiotherapy, and chemotherapy, significantly enhancing the antitumor efficacy. This positions MgH_2 microspheres as a promising candidate with substantial potential for clinical application.

4. Experimental

4.1 Chemicals and reagents

Barium nitrate ($Ba(NO_3)_2$), sodium hydroxide (Na(OH)), titanium butoxide ($Ti(OBu)_4$), *N*-methyl pyrrolidone (NMP), 1-butanol, *n*-hexane and ethanol (C_2H_5OH) were purchased from Aladdin. DNase I recombinant and oleic acid (OA) were purchased from Sigma-Aldrich. D-Luciferin, JC-10 assay, Calcein-AM/PI, methylene blue (MB), polyethylene glycol 200 (PEG 200) and CCK8 were purchased from Solarbio. DCFH-DA and Annexin V-APC/PI Apoptosis Kit were purchased from Beyotime. Polycaprolactone (PCL, M_W: 80 000) was purchased from Macklin. The antibodies were purchased from BioLegend Inc. Collagenase type IV was purchased from Gibco. All reagents were used as received without further purification.

4.2 Materials preparation

Preparation of BTO nanoparticles. The BTO NPs were synthesized through hydrothermal method as described in the previous study. In brief, 1 mmol $Ba(NO_3)_2$ and 12.5 mmol NaOH were dissolved in 5 mL deionized water, respectively. Then, 1 mmol $Ti(OBu)_4$ and 2.5 mmol OA were dispersed in 5 mL 1-butanol, respectively. The above-mentioned solutions were mixed and the reaction was carried out at 135 °C for 18 h. After cooling, the mixture was centrifuged at 8000 rpm for 5 min, washed three times with hexane and ethanol (hexane : ethanol = 1 : 5), and dried under vacuum.

Preparation of FITC-conjugated BTO nanoparticles. A mixture containing 70 mg DSPE-PEG2000-FITC, 50 mg BTO, and 500 μL tetrahydrofuran (THF) was dispersed in 10 mL deionized water under ultrasonication for 30 min, followed by continuous magnetic stirring (800 rpm) at room temperature for 12 h. The resulting FITC-BTO nanoparticles were subsequently collected by centrifugation (12 000 rpm, 15 min) and washed three times with deionized water to remove the unreacted components.

Preparation of MgH_2-PCL microspheres. MgH_2 particles with a small diameter were obtained through the liquid-phase exfoliation method. Briefly, MgH_2 powder was dispersed in NMP firstly, and then the mixed solution was treated with an ultrasonic probe for 8 h at 4 °C. Subsequently, the treated solution was placed in a constant temperature ultrasonic water bath at 4 °C overnight. Finally, the mixed solution was centrifuged at 12 000 rpm for 30 min to obtain MgH_2 nanoparticles. The obtained MgH_2 nanoparticles were washed with C_2H_5OH several times and dried in a vacuum drying oven. The 3% PCL solution was obtained by dissolving 0.3 g PCL in 10 mL dichloromethane, and the washed 75 mg MgH_2 particles were subsequently dispersed in this solution. An electrospinning machine was used to obtain microspheres (containing 20% MgH_2) at a high voltage of 12 kV and a flow rate of 1.2 cm h^{-1}.

4.3 Characterization

The morphologies and elemental mapping of the microspheres were observed by SEM (SU8020, Hitachi, Japan). The microscopic morphology and structure of BTO were observed through TEM and HRTEM (Tecnai G2 F20 STWIN TMP, FEI, USA). The phase structures of BTO NPs and MgH_2 NPs were analyzed by XRD (X'Pert, PANalytical, Netherlands) with a Cu Kα source. The absorbance spectra were recorded using a UV-vis-NIR spectrophotometer (UV3600, SHIMADZU, Japan) at room temperature. The molecular structure of BTO was

observed by Raman spectrometer (LabRAM HR Evolution, HORIBA JY, France).

4.4 Measurement of H_2 release and pH variation

Under the catalysis of a Pt catalyst, MB can quickly and easily detect the generation of H_2. 10 mg MgH_2 microspheres was dispersed in an MB–Pt solution (10 μg mL^{-1} MB and 60 μg mL^{-1} Pt), and then the absorbance was measured at different times using a UV-vis-NIR spectrophotometer. H_2 generation was quantified by gas chromatography (GC-7820, HUIFEN, China). 10 mg microspheres was dispersed in headspace vials with headspace caps containing 2 mL 1 × PBS, and 400 μL of gas was injected into the gas chromatograph at different time points (every 3 h) to determine the H_2 concentration. The microspheres were co-cultured with tumor cells for 24 h and the supernatant was collected to be measured using pH meter (FiveEasy Plus, METTLER TOLEDO, USA).

4.5 *In vitro* ROS generation

20 mg BTO nanoparticles was mixed with 5 mL MB solution (5 μg mL^{-1}) overnight to achieve dissociation adsorption equilibrium. After US irradiation (1 MHz, 1 W cm^{-2}, 50% duty cycle), the supernatant was withdrawn to measure the absorption. The whole degradation experiment was carried out under dark conditions.

4.6 ESR measurement

The trapping agent DMPO (5,5-dimethyl-1-pyrroline N-oxide) (Sigma) was employed to detect generated ROS. 200 μL BTO (5 mg mL^{-1}) was mixed with 10 μL DMPO under US irradiation (1.2 W cm^{-2}, 50% duty cycle, 5 min and 10 min), respectively. The characteristic $^{\bullet}OH$ signals were subsequently detected using an ESR spectrometer (A300-10/12, Bruker, Germany).

4.7 Cellular experiments

The murine mammary carcinoma 4T1 cells, melanoma B16F10 cells, colon cancer CT26 and HaCat cells were cultured in the DMEM media (Solarbio, China) containing 10% fetal bovine serum (FBS, Gibco) and 1% penicillin–streptomycin liquid (Solarbio, China) at 37 °C under 5% CO_2.

4.8 Biocompatibility tests

B16F10 cells were seeded in 96-well plates (Corning, USA) at a density of 8×10^3 cells per well. Then, the B16F10 cells were co-cultured with varying concentrations of MgH_2 (0, 100, 300, 500, and 700 μg mL^{-1}) at 37 °C for 24 h. HaCat cells (at a density of 8×10^3 cells per well) were seeded in 96-well plates (Corning, USA) and co-cultured with varying concentrations of MgH_2 (0, 100, 200, 300, and 400 μg mL^{-1}) and BTO (0, 50, 100, 200, and 500 μg mL^{-1}) at 37 °C for 24 h. 200 μL of medium containing 10% CCK8 reagent was added and incubated for one hour at 37 °C. The absorbance was measured at 450 nm and 650 nm using a microplate reader (Varioskan LUX, ThermoFisher Scientific).

4.9 *In vitro* cytotoxicity tests

B16F10 cells (at a density of 8×10^3 cells per well) were seeded in 96-well plates overnight and set into eight groups, as follows: (1) control group, (2) control + US group, (3) BTO group, (4) BTO + US group, (5) MgH_2 group, (6) MgH_2 + US group, (7) BTO + MgH_2 group, and (8) BUM group. 4T1 and CT26 cells (at a density of 8×10^3 cells per well) were seeded in 96-well plates (Corning, USA) overnight and set into five groups, as follows: (1) control group, (2) control + US group, (3) BTO group, (4) BTO + US group, and (5) BUM group. After being co-cultured with different materials (BTO: 100 μg mL^{-1}; MgH_2: 300 μg mL^{-1}) for 4 h, the tumor cells were exposed to US (1 MHz, 1 W cm^{-2}, 50% duty cycle) for 5 min. Then, the cells were incubated at 37 °C for another 18 h. The cell viability was tested with the CCK8 assay.

4.10 *In vitro* ROS detection and cytotoxicity profiles

B16F10 cells (at a density of 5×10^3 cells per well) were seeded in 96-well plates overnight and set into six groups, as follows: (1) control group, (2) control + US group, (3) BTO group, (4) BTO + US group, (5) BTO + MgH_2 group, and (6) BUM group.

The DCFH-DA probe was used to assess intracellular ROS generation. After being co-cultured with different materials (BTO: 100 μg mL^{-1}; MgH_2: 300 μg mL^{-1}) for 4 h, the cells were cocultured with 100 μL of FBS-free DMEM medium containing DCFH-DA (10 μmol L^{-1}) for 15 min. Next, the tumor cells were exposed to US (1 MHz, 1 W cm^{-2}, 50% duty cycle) for 5 min. Then, the cells were rinsed with PBS. The intracellular ROS production was observed using a fluorescence microscope (DM6000, Leica, Germany).

Calcein-AM/PI solution was used to visualize the cytotoxicity profiles. After being co-cultured with different materials (BTO: 100 μg mL^{-1}; MgH_2: 300 μg mL^{-1}) for 4 h, the tumor cells were exposed to US (1 MHz, 1 W cm^{-2}, 50% duty cycle) for 5 min. Then, the cells were incubated at 37 °C for another 18 h. Finally, the treated cells were rinsed with PBS and stained with Calcein-AM/PI solution. Fluorescence imaging was performed using a fluorescence microscope.

4.11 Detection of MMP and quantitative analysis of apoptosis

B16F10 cells (at a density of 1×10^5 cells per well) were cultured in a confocal glass bottom dish overnight and set into four groups, as follows: (1) control group, (2) MgH_2 group, (3) BTO + US group, and (4) BUM group. After being co-cultured with different materials (BTO: 100 μg mL^{-1}; MgH_2: 300 μg mL^{-1}) for 4 h, the B16F10 cells were exposed to US (1 MHz, 1 W cm^{-2}, 50% duty cycle) for 5 min.

To observe the change in intracellular MMP, the treated cells were stained with JC-10 dye according to the manufacturer's protocols. Images were acquired using a confocal laser scanning microscope (CLSM) (TCS SP8, Leica, Germany).

To quantify the cell apoptosis, the supernatant and adherent cells after the treatment were collected. Then the Annexin V-APC/PI Detection Kit (Multi sciences) was used to stain the

collected cells. Finally, cell apoptosis was quantified *via* flow cytometry (CytoFLEX, Beckman Coulter, USA).

4.12 Detection of intracellular ATP

B16F10 cells were seeded in 6-well plates at a density of 4×10^5 cells per well and set into four groups, follows: (1) control group, (2) MgH_2 group, (3) BTO + US group, and (4) BUM group. After being co-cultured with different materials (BTO: 100 μg mL^{-1}; MgH_2: 300 μg mL^{-1}) for 4 h, the B16F10 cells were exposed to US (1 MHz, 1 W cm^{-2}, 50% duty cycle) for 5 min. After incubation for 4 h, the supernatant was collected by lysing the cells and the ATP content was detected and calculated through the ATP assay kit.

4.13 Biodistribution of FITC-conjugated BTO nanoparticles *in vivo*

FITC-conjugated BTO (10 mg kg^{-1}) was injected into the tumor. 24 h after BTO injection, the treated mouse was euthanized, and then the excised tumor tissues were fixed in 4% paraformaldehyde (PFA) at 4 °C for 2 h, followed by cryoprotection in 30% sucrose solution for 10 h at 4 °C. Then, the samples were embedded in optimal cutting temperature compound (OCT) and sectioned at 30-μm thickness using a cryostat (Leica CM1950). The distribution of nanoparticles within the tumor sections was analyzed by confocal laser scanning microscopy.

4.14 Expression of inflammatory factors in macrophage

TNF-α, IL-6 and IL-1β were visualized using immunocytochemical staining. RAW 264.7 cells were divided into six groups, as follows: (1) Blank group (with medium only), (2) control group, (3) MgH_2 group, (4) BTO + US group, (5) BUM group, and (6) LPS group (1 μg mL^{-1}). The bone marrow-derived macrophages were divided into six groups, as follows: (1) blank group (with medium only), (2) control group, (3) MgH_2 group, (4) BTO + US group, and (5) BUM group. The B16F10 cells were seeded onto 6-well plates with 4×10^5 cells per well and set into four groups, as follows: (1) control group, (2) MgH_2 group, (3) BTO + US group, and (4) BUM group. After being co-cultured with different materials (BTO: 100 μg mL^{-1}; MgH_2: 300 μg mL^{-1}) for 4 h, the B16F10 cells were exposed to US (1 MHz, 1 W cm^{-2}, 50% duty cycle) for 5 min. After incubation for 24 h, the supernatant was collected and co-cultured with macrophage cells for 48 h. Then, the cells were thoroughly washed in PBS and fixed with 4% formaldehyde. The fixed cells were blocked in 5% goat serum for 1 h at room temperature, and then incubated overnight with the primary antibodies for TNF-α, IL-6 or IL-1β (Abcam) in 5% goat serum. Then, the cells were incubated with appropriate secondary antibodies for 2 h at room temperature in the dark, before being incubated with DAPI for 10 min. Finally, images were captured using CLSM.

4.15 *In vivo* systemic therapy induced by the materials

All animal experiments were approved by the Committee on Ethics of the Beijing Institute of Nanoenergy and Nanosystems (2023029LZ), and all animal procedures were carried out in accordance with the national standards of Laboratory Animal Requirements of Environment and Housing Facilities (GB14925-2001). 50 μL CT26 cells (1×10^5 cells) was seeded subcutaneously on the right back of Balb/c mice to establish the tumor model. 7 days later (it was observed that the tumor had formed, but its volume was difficult to measure at this time, the volume was recorded as 0), the mice were randomly divided into four groups ($n = 5$), as follows: (1) control group, (2) MgH_2 group, (3) BTO + US group, and (4) BUM group. PEG-200 with and without different materials were injected into the tumor (BTO: 10 mg kg^{-1}; MgH_2 microspheres: 130 μg per mouse). 4 h after BTO injection, US (1 MHz, 1 W cm^{-2}, 50% duty cycle, 8 min) irradiation was conducted. In the therapeutic process, the body weight and tumor volume of the mice were monitored every two days. The tumor volume was calculated according to the following formula:

$$V\,(mm^3) = L \times W^2/2 \text{ (}L\text{: length, }W\text{: width)}$$

At the end of the experiment, the treated mice in each group were euthanized, and all the tumors were harvested and photographed. Then, the organs and tumors were fixed with 10% formalin and stained with H&E, TUNEL and Ki-67 for histopathological analysis.

Blood samples were obtained from the orbit for blood biochemistry tests, which were conducted using a hematology analyzer (Celltac Es, Nihon Kohden, Japan). CT26 tumor-bearing mice were injected with MgH_2 microspheres, and then imaged under a Vevo LAZR small animal ultrasonic imaging system for *in vivo* ultrasonic imaging. The mice were sacrificed when their tumor size reached over 2000 mm^3.

4.16 Detection of cytokines

Mice bearing CT26 tumors were divided into four groups and treated as described above. After treatments for 4 days, the mice were sacrificed. The tumors were collected and homogenized in ice-cold PBS (1 : 9 w/v), followed by ultrasonication. The lysates were centrifuged at 12,000 rpm for 20 min at 4 °C, and the supernatants were analyzed for cytokine content using commercial ELISA kits according to the manufacturer's protocol.

4.17 *In vivo* immunoassays

Mice bearing CT26 tumors were divided into four groups and treated as described above. After treatments for 7 days, the mice were sacrificed. The tumors and lymph nodes were collected and digested into single-cell suspensions with PBS containing 0.2% collagenase type IV and 100 U mL^{-1} DNase I recombinant for 2 h under 37 °C. Then, the cells were resuspended in PBS and stained with antibodies. All antibodies were diluted 200 times before staining. The stained cells were quantified by the flow cytometry and analyzed using the FlowJo software (version 10.8.1,TreeStar).

4.18 *In vivo* systemic therapy induced by the materials combined with aPD-1

50 μL CT26 cells (5×10^5 cells) were seeded subcutaneously on the right back of Balb/c mice to establish the tumor model.

When the tumors of the mice reached about 100 mm^3, the mice were divided into four groups (n = 4), as follows: (1) control group, (2) aPD-1 group, (3) BUM group, and (4) BUM + aPD-1 group. On day 0, 2, and 4, BTO (10 mg kg^{-1} per mouse each time) was injected into the tumor with US irradiation (1 MHz, 1 W cm^{-2}, 50% duty cycle, 8 min, 4 h after BTO injection). The MgH_2 microspheres (130 μg per mouse per time) were injected into the tumor at day 1, 3, and 5. Also, aPD-1 (20 μg per mouse per time) was intravenously injected at day 2, 4, and 6. D-Luciferin was injected intraperitoneally, and then *in vivo* bioluminescence images of the mice bearing subcutaneous CT26 tumors were obtained through a small animal live imaging system (IVIS Lumina III, PerkinElmer, USA) at day 0, 3, and 6. The tumor sizes and the body weights of the mice were monitored every other day.

4.19 Statistical analysis

All results were statistically analyzed and reported as mean ± SD. The P value was determined using One-way ANOVA with Tukey's multiple comparison test ($^*P < 0.05$, $^{**}P < 0.01$, $^{***}P < 0.001$, and $^{****}P < 0.0001$) with GraphPad Prism 8.0 software.

Author contributions

J. H. and L. X. designed and conducted most of the experiments and analyzed the data. J. M., Y. F., and D.L. contributed to material fabrication and characterization. X. W., E. W. and H. F. assisted with the animal experiments. J. H., L. X. wrote the manuscript. Z. L. supervised the project. L. X., Z. L. reviewed and revised the manuscript. All authors discussed the results and approved the final manuscript.

Conflicts of interest

There are no conflicts to declare.

Data availability

Data supporting the results of this study can be obtained from the corresponding author upon request.

Acknowledgements

The authors thank all laboratory members for their cooperation in this study. This study was supported by the Natural Science Foundation of Beijing Municipality (L245015, Z240022), the National Natural Science Foundation of China (82202075, T2125003), and the Fundamental Research Funds for the Central Universities.

Notes and references

1 E. Musielak and V. Krajka-Kuźniak, *Micro*, 2025, **5**, 2.
2 Y. Shan, L. Xu, X. Cui, E. Wang, F. Jiang, J. Li, H. Ouyang, T. Yin, H. Feng, D. Luo, Y. Zhang and Z. Li, *Mater. Horiz.*, 2024, **11**, 1032–1045.
3 S. Lyu, Z. Chen, Y. Ding and Y. Wang, *Device*, 2024, **2**, 100423.
4 R. Ghanim, A. Kaushik, J. Park and A. Abramson, *Device*, 2023, **1**, 100092.
5 P. Zhu, Y. Chen and J. Shi, *Adv. Mater.*, 2020, **32**, 2001976.
6 H. Wang, A. J. Najibi, M. C. Sobral, B. R. Seo, J. Y. Lee, D. Wu, A. W. Li, C. S. Verbeke and D. J. Mooney, *Nat. Commun.*, 2020, **11**, 5696.
7 H. Cheng, Y. Qiu, Y. Xu, L. Chen, K. Ma, M. Tao, L. Frankiw, H. Yin, E. Xie, X. Pan, J. Du, Z. Wang, W. Zhu, L. Chen, L. Zhang and G. Li, *Nat. Metab.*, 2023, **5**, 314–330.
8 Q. Tang, S. Sun, P. Wang, L. Sun, Y. Wang, L. Zhang, M. Xu, J. Chen, R. Wu, J. Zhang, M. Gong, Q. Chen and X. Liang, *Adv. Mater.*, 2023, **35**, 2300964.
9 Y. Kang, Z. Mao, Y. Wang, C. Pan, M. Ou, H. Zhang, W. Zeng and X. Ji, *Nat. Commun.*, 2022, **13**, 2425.
10 Y. Fan, J. Ye, Y. Kang, G. Niu, J. Shi, X. Yuan, R. Li, J. Han and X. Ji, *Sci. Adv.*, 2024, **10**, eadm9561.
11 V. S. Pelly, A. Moeini, L. M. Roelofsen, E. Bonavita, C. R. Bell, C. Hutton, A. Blanco-Gomez, A. Banyard, C. P. Bromley, E. Flanagan, S.-C. Chiang, C. Jørgensen, T. N. Schumacher, D. S. Thommen and S. Zelenay, *Cancer Discovery*, 2021, **11**, 2602–2619.
12 Z. Li, M. Yuan, H. R. Liu, C. Liu, J. H. Zhang, Y. F. Guo, Y. F. Li, Y. C. He, X. W. Zhang and D. W. Gao, *Adv. Funct. Mater.*, 2025, 2419032.
13 A. B. Wu, L. D. Jiang, C. Xia, Q. Q. Xu, B. Zhou, Z. K. Jin, Q. J. He and J. X. Guo, *Adv. Sci.*, 2023, **10**, 2303016.
14 R. Zhang, Q. Wang, J. J. Pan, J. Du, H. Yang, B. F. Wang, Y. H. Li, Y. Q. Miao, X. M. Hou, J. X. Wu and Q. Miao, *Adv. Sci.*, 2025, **12**, 2413519.
15 H. Yan, M. Fan, H. Liu, T. Xiao, D. Han, R. Che, W. Zhang, X. Zhou, J. Wang, C. Zhang, X. Yang, J. Zhang and Z. Li, *J. Nanobiotechnol.*, 2022, **20**, 280.
16 L. Xiao, X. Li, J. Zhang and Z. He, *ACS Appl. Nano Mater.*, 2021, **4**, 12779–12787.
17 Y. Wu, M. Yuan, J. Song, X. Chen and H. Yang, *ACS Nano*, 2019, **13**, 8505–8511.
18 F. Gong, J. Xu, B. Liu, N. Yang, L. Cheng, P. Huang, C. Wang, Q. Chen, C. Ni and Z. Liu, *Chem*, 2022, **8**, 268–286.
19 N. Yang, F. Gong, B. Liu, Y. Hao, Y. Chao, H. Lei, X. Yang, Y. Gong, X. Wang, Z. Liu and L. Cheng, *Nat. Commun.*, 2022, **13**, 2336.
20 X. Yao, D. Chen, B. Zhao, B. Yang, Z. Jin, M. Fan, G. Tao, S. Qin, W. Yang and Q. He, *Adv. Sci.*, 2022, **9**, 2101965.
21 Y. He, X. Tian, X. Fan, X. Gong, S. Tan, A. Pan, S. Liang, H. Xu and F. Zhou, *ACS Appl. Mater. Interfaces*, 2023, **15**, 552–565.
22 S. Chen, Y. Zhu, Q. Xu, Q. Jiang, D. Chen, T. Chen, X. Xu, Z. Jin and Q. He, *Nat. Commun.*, 2022, **13**, 5684.
23 Y. Zhu, Q. Jiang, Z. Jin, D. Chen, Q. Xu, J. Chen, Y. Zeng, S. Chen and Q. He, *Adv. Healthcare Mater.*, 2023, **12**, 2201705.

24 M. Xu, Y. Zhou, C. Ren, X. Liang and N. Li, *Adv. Funct. Mater.*, 2021, **31**, 2104892.
25 S. Wang, K. Liu, Q. Zhou, C. Xu, J. Gao, Z. Wang, F. Wang, B. Chen, Y. Ye, J. Ou, J. Jiang, D. A. Wilson, S. Liu, F. Peng and Y. Tu, *Adv. Funct. Mater.*, 2021, **31**, 2009475.
26 L. Zhang, P. Zhao, C. Yue, Z. Jin, Q. Liu, X. Du and Q. He, *Biomaterials*, 2019, **197**, 393–404.
27 C. Xu, S. Wang, H. Wang, K. Liu, S. Zhang, B. Chen, H. Liu, F. Tong, F. Peng, Y. Tu and Y. Li, *Nano Lett.*, 2021, **21**, 1982–1991.
28 I. Ohsawa, M. Ishikawa, K. Takahashi, M. Watanabe, K. Nishimaki, K. Yamagata, K.-i Katsura, Y. Katayama, S. Asoh and S. Ohta, *Nat. Med.*, 2007, **13**, 688–694.
29 S. Chen, Y. Yu, S. Xie, D. Liang, W. Shi, S. Chen, G. Li, W. Tang, C. Liu and Q. He, *Nat. Commun.*, 2023, **14**, 7783.
30 M. Otsuka, K. Arai, T. Yoshida and A. Hayashi, *Graefe's Arch. Clin. Exp. Ophthalmol.*, 2024, **262**, 1011.
31 N. Yang, S. Sun, J. Xu, F. Gong, H. Lei, Y. Hao, Z. Pei, C. Wang, Q. Yu, J. Nie, N. Jiang, C. Ni and L. Cheng, *Adv. Mater.*, 2025, **37**, 2414929.
32 M. Yuan, S. Liang, L. Yang, F. Li, B. Liu, C. Yang, Z. Yang, Y. Bian, P. a Ma, Z. Cheng and J. Lin, *Adv. Mater.*, 2023, **35**, 2209589.
33 G. Qi, T. Yu, J. Li, Z. Guo, K. Ma and Y. Jin, *Adv. Mater.*, 2023, **35**, 2208414.
34 J. Chen, S. Lin, D. Zhao, L. Guan, Y. Hu, Y. Wang, K. Lin and Y. Zhu, *Adv. Funct. Mater.*, 2021, **31**, 2006853.
35 M. Xu, G. Wu, Q. You and X. Chen, *Adv. Sci.*, 2024, **11**, 2401310.
36 P. Zhao, Z. Jin, Q. Chen, T. Yang, D. Chen, J. Meng, X. Lu, Z. Gu and Q. He, *Nat. Commun.*, 2018, **9**, 4241.
37 R. Sun, X. Liu, G. Li, H. Wang, Y. Luo, G. Huang, X. Wang, G. Zeng, Z. Liu and S. Wu, *ACS Nano*, 2020, **14**, 8135–8148.
38 Y. Wang, Y. Liu, J.-e Zhou, L. Lin, C. Jia, J. Wang, L. Yu, Y. Wang and Z. Yan, *Chem. Eng. J.*, 2021, **421**, 129917.
39 C. Zhang, D.-W. Zheng, C.-X. Li, M.-Z. Zou, W.-Y. Yu, M.-D. Liu, S.-Y. Peng, Z.-L. Zhong and X.-Z. Zhang, *Biomaterials*, 2019, **223**, 119472.
40 R. Zan, H. Wang, W. Cai, J. Ni, B. J. C. Luthringer-Feyerabend, W. Wang, H. Peng, W. Ji, J. Yan, J. Xia, Y. Song and X. Zhang, *Bioact. Mater.*, 2022, **9**, 385–396.
41 L. Ren, Y. Li, N. Zhang, Z. Li, X. Lin, W. Zhu, C. Lu, W. Ding and J. Zou, *Nano-Micro Lett.*, 2023, **15**, 93.
42 J. Lötscher, A.-A. Martí i Líndez, N. Kirchhammer, E. Cribioli, G. M. P. Giordano Attianese, M. P. Trefny, M. Lenz, S. I. Rothschild, P. Strati, M. Künzli, C. Lotter, S. H. Schenk, P. Dehio, J. Löliger, L. Litzler, D. Schreiner, V. Koch, N. Page, D. Lee, J. Grählert, D. Kuzmin, A.-V. Burgener, D. Merkler, M. Pless, M. L. Balmer, W. Reith, J. Huwyler, M. Irving, C. G. King, A. Zippelius and C. Hess, *Cell*, 2022, **185**, 585–602.
43 J. Xue, T. Wu, Y. Dai and Y. Xia, *Chem. Rev.*, 2019, **119**, 5298–5415.
44 T. Xu, Y. Yang, D. Suo, H. P. Bei, X. Xu and X. Zhao, *Small*, 2022, **18**, 2205695.
45 P. Wang, Q. Tang, L. Zhang, M. Xu, L. Sun, S. Sun, J. Zhang, S. Wang and X. Liang, *ACS Nano*, 2021, **15**, 11326–11340.
46 F. Gong, L. Cheng, N. Yang, Y. Gong, Y. Ni, S. Bai, X. Wang, M. Chen, Q. Chen and Z. Liu, *Nat. Commun.*, 2020, **11**, 3712.
47 J. Shen, Y. He, J. Wu, C. Gao, K. Keyshar, X. Zhang, Y. Yang, M. Ye, R. Vajtai, J. Lou and P. M. Ajayan, *Nano Lett.*, 2015, **15**, 5449–5454.
48 Y.-N. Liu, X. Zhou, X. Wang, K. Liang, Z.-K. Yang, C.-C. Shen, M. Imran, S. Sahar and A.-W. Xu, *RSC Adv.*, 2017, **7**, 30080–30085.
49 Z. Dai, Q. Zhang, X. Li, Q. Chen, J. Chen, M. Wang and H. Chen, *Mater. Today*, 2023, **65**, 62–77.
50 I. Martins, Y. Wang, M. Michaud, Y. Ma, A. Q. Sukkurwala, S. Shen, O. Kepp, D. Métivier, L. Galluzzi, J. L. Perfettini, L. Zitvogel and G. Kroemer, *Cell Death Differ.*, 2014, **21**, 79–91.
51 L. Liu, Y. Wu, J. Ye, Q. Fu, L. Su, Z. Wu, J. Feng, Z. Chen and J. Song, *Chem*, 2022, **8**, 2990–3007.
52 Y.-X. Zhang, Y.-Y. Zhao, J. Shen, X. Sun, Y. Liu, H. Liu, Y. Wang and J. Wang, *Nano Lett.*, 2019, **19**, 2774–2783.
53 S. Sun, Q. Tang, Y. Wang, L. Zhang, J. Chen, M. Xu, L. Sun, L. Cui and X. Liang, *ACS Appl. Mater. Interfaces*, 2022, **14**, 27013–27027.
54 H. Zhao, B. Zhao, L. Li, K. Ding, H. Xiao, C. Zheng, L. Sun, Z. Zhang and L. Wang, *Adv. Healthcare Mater.*, 2020, **9**, 1901335.